# Aerodynamic Interactions of Side-by-Side Rotors in Ground Proximity

Dekker, Hasse N.J.; Ragni, Daniele; Baars, Woutijn J.; Scarano, Fulvio; Tuinstra, Marthijn

**DOI**
10.2514/1.J061105

**Publication date**
2022

**Document Version**
Final published version

**Published in**
AIAA Journal

AIAA JOURNAL
Vol. 60, No. 7, July 2022

# Aerodynamic Interactions of Side-by-Side Rotors in Ground Proximity

Hasse N. J. Dekker,* Daniele Ragni,† Woutijn J. Baars,‡ and Fulvio Scarano§
*Delft University of Technology, 2629 HS Delft, The Netherlands*
and
Marthijn Tuinstra¶
*Royal Netherlands Aerospace Centre, 8316 PR Marknesse, The Netherlands*

https://doi.org/10.2514/1.J061105

**An experimental investigation is conducted to study the aerodynamic behavior of a two-rotor system in ground proximity. The counter-rotating rotors are placed side-by-side in the hovering condition. The time-averaged and unsteady flow behavior is studied when the rotor-to-rotor lateral distance and the distance between the rotors and the ground are varied. The experiments are performed using three-dimensional large-scale volumetric velocimetry with helium-filled soap bubbles as tracers, tracked by the particle motion analysis technique "Shake-The-Box." The mean velocity field reveals the wake deflection due to the ground plane and the formation of toroidal-shape regions of separated flow below each rotor. The interaction of the wall jets formed by slipstream deflection results in a separation line with the flow emerging from the wall in a fountain-like pattern. Regimes of flow re-ingestion occur when the rotors are sufficiently far apart. The flowfield exhibits the tendency toward asymmetric states, during which the fountain flow column and the domain of re-ingestion shift closer to one of the rotors. A generic classification of flow regimes is proposed in relation to the behavior of two rotors in ground effect.**



## Nomenclature

| | | |
|---|---|---|
| $B$ | = | number of rotor blades |
| $C_t$ | = | thrust coefficient |
| $D$ | = | rotor diameter, mm |
| $f$ | = | focal length, mm |
| $f_\#$ | = | numerical aperture |
| $H$ | = | rotor-to-ground standoff distance, mm |
| $h$ | = | grid spacing, mm |
| $J$ | = | advance ratio |
| $L$ | = | characteristic length of measurement domain, mm |
| $M_{\text{tip}}$ | = | tip Mach number |
| $R$ | = | rotor radius, mm |
| $Re_c$ | = | chord-based Reynolds number |
| $S$ | = | tip-to-tip rotor separation distance, mm |
| $T$ | = | thrust, N |
| TKE | = | normalized turbulent kinetic energy |
| $U_{\text{tip}}$ | = | rotor tip speed, m/s |
| $v$ | = | lateral velocity, m/s |
| $W_{\text{ind}}$ | = | hover induced velocity, m/s |
| $w$ | = | axial velocity, m/s |
| $\delta t$ | = | pulse width, μs |
| $\Omega$ | = | rotational speed, Hz |

*Subscript*

| | | |
|---|---|---|
| tip | = | blade tip condition |

Received 25 July 2021; revision received 2 February 2022; accepted for publication 2 February 2022; published online 28 February 2022. 

*Ph.D. Candidate, Wind Energy, Faculty of Aerospace Engineering; h.n.j.dekker-1@tudelft.nl. Member AIAA.
†Associate Professor, Wind Energy, Faculty of Aerospace Engineering; d.ragni@tudelft.nl. Member AIAA.
‡Assistant Professor, Aerodynamics, Faculty of Aerospace Engineering; w.j.baars@tudelft.nl. Senior Member AIAA.
§Full Professor, Aerodynamics, Faculty of Aerospace Engineering; f.scarano@tudelft.nl. Member AIAA.
¶Scientist Principal Aeroacoustics, Vertical Flight and Aeroacoustics Department; marthijn.tuinstra@nlr.nl. Member AIAA.

## I. Introduction

HOVERING counter-rotating side-by-side rotors are found in several aircraft configurations (e.g., drones, tilt-rotors, tilt wings, and distributed propulsion concepts [1]). A number of studies [2–9] focusing on rotor-to-rotor interactions show that the distance between the rotors has a relatively small influence on their mean thrust coefficient. However, strong temporal variations of the aerodynamic loading have been reported by Ning [5], Ning and associates [7], and Alvarez and Ning [9]. In the latter study an increase of the thrust fluctuations of up to 250%, compared to a single rotor, was found for a side-by-side rotor configuration with a tip-to-tip spacing $S$ of $0.1R$ (see Fig. 1a for relevant parameters). This effect is caused by an interaction between the radial velocities in the slipstream, forming an upwash between the individual wakes [3,7]. At this rotor separation distance, vortical structures are also found at the inflow of the rotors [8]. Moreover, an overall noise level increase of 3 dB has been reported for side-by-side rotors with $S/R = 0.1$, compared to the same system with a separation distance of $S/R = 1.0$, which has been ascribed to unsteady loading [5–7].

During takeoff and landing the rotors hover in close proximity to the ground. This creates a wake organization that deviates from the widely used Landgrebe wake model [10]. Ground effect conditions have been studied extensively for single rotors [11–13], whereby the rotor slipstream undergoes a rapid deflection due to the presence of the ground plane, resulting in a radially spreading turbulent wall jet. Due to the nonuniform induced velocity by the rotor, the flow stagnates below the rotor hub, causing a toroidal separation region [14]. When a second rotor is introduced in a side-by-side configuration, at the same wall distance, an interaction has been observed between the two rotor-induced wall jets. The resulting flowfield loses axial symmetry and becomes planar-symmetric around the plane that separates the two rotors.

Studies of multirotor systems in ground effect are particularly relevant for the controllability and safe operation of drones [15]. The rotor spacing $S$ and the ground standoff distance $H$ normalized to the rotor radius $R$ have been recognized as the parameters dominating the aeropropulsive behavior of such systems [16]. Depending on the rotor spacing, a nonlinear variation in the thrust as a function of $S$ and $H$ occurs [17]. The behavior deviates from the trend that is predicted by classical ground effect models applied to helicopter configurations [18].

Multirotor systems in ground effect have been reported to deliver additional thrust enhancement (ratio between in- and out-of-ground

thrust) of up to 30%, compared to the single rotor [15,19]. In contrast, a recent study by He and Leang [16] reports a sudden drop in thrust for $S/R = 2$ and $H/R = 2$ of 8% below the free-hover condition. Such nonlinear behavior needs to be taken into account for the controllability of multirotor aerial vehicles during takeoff, landing, and hovering near the ground. The physical root cause of such behavior has been ascribed to the onset of global flow recirculation with upward flow between the rotors, known as the fountain flow [15,19], which under certain conditions causes the turbulent fountain flow to be re-ingested into the rotors [16,17]. The fountain flow and re-ingestion mechanisms are schematically illustrated in Fig. 1b. Furthermore, ingestion of highly turbulent flow is associated to unsteady blade loading, in turn yielding thrust fluctuations and additional sources of noise [20]. Notably, He and Leang [16] identified contradictions among experiments carried out by different researchers, about the role of rotor spacing, the fountain flow, and performance of rotor systems in ground effect. Whereas two studies, one aimed at rotor–obstacle interaction [21] and another researching a quad-rotor configuration [22], reported an increase of the thrust coefficient with a larger rotor spacing, another investigation reported the opposite behavior [23]. He and Leang [16] link these apparent discrepancies to the fact that for relatively closely spaced rotors, an increase in rotor separation distance $S$ results in a decrease in the thrust, whereas this effect is opposite for a relatively large spacing of the rotors.

To date, the re-ingestion condition for a multirotor system has only been hypothesized on the basis of the measured thrust perturbations. A proof of the mechanism based on quantitative flow visualization along with detailed information that characterizes the unsteadiness of the (three-dimensional [3D]) velocity field is missing. A comprehensive understanding of the mechanisms behind the formation of the fountain flow and the flow re-ingestion is key to justify the observed differences in propulsive thrust and predict both the mean and unsteady behavior of multirotor systems hovering in ground effect. Therefore, the goal of the current study is to assess the 3D flow pattern associated with a two-rotor system in ground effect, with focus toward the identification of global flow regimes that depend upon rotor separation and ground standoff proximity. Moreover, the characterization of large-scale unsteady behavior is explored. To this purpose, volumetric velocity measurements are performed using large-scale Particle Image Velocimetry (PIV) in a domain that encompasses the two rotors and a ground plane. The experiments make use of helium-filled soap bubbles (HFSBs) [24] as flow tracers, whereas the illumination and imaging follow the principles of tomography. The analysis of the recordings to extract the tracers' motion is conducted with the "Shake-The-Box" algorithm [25].

The outline of the paper is as follows. Section II describes the experimental apparatus, the measurement system, and the data processing. A discussion of the time-averaged flow topology is given in Sec. III. Section IV presents a parametric study on the effect of rotor spacing and height. In this section a synthesis of the results is provided where the identified flow regimes are categorized in a parametric space. Finally, Sec. V presents some observations of the temporal dynamics of the rotor wakes and the emerging fountain flow.

## II. Experimental Arrangement

### A. Side-by-Side Rotor System

Two counter-rotating rotors are installed with their axes perpendicular to a ground plane. The two-blade twisted rotors comprise a radius of $R = 76.2$ mm, a pitch of 4 inches, and a parabolic tip. The APC-brand rotors are commercially available, and their model numbers are APC 6X4E and APC 6X4EP (identical but mirrored, for the counter-rotating configuration). Each rotor is driven by a geared in-runner brushless motor (type Hacker, B20 26 L kv2020+4:1) operated at a shaft rotation speed of $\Omega = 167$ Hz. The rotors are not phase-controlled, which means that the relative phase difference varies during acquisition. The discrepancy in rotational speed between the rotors is estimated to be equal to 0.25 Hz, resulting in a variation of the phase difference between the rotor blades, over the acquisition duration of the measurement. Hence, in the time-averaged sense, the measurement can be considered as one with a random phase between the blades. The Reynolds number, based on the sectional chord length at a nominal radius of $0.75R$, is $Re_c = 42{,}000$ and the tip Mach number is $M_{\text{tip}} = 0.22$. The rotors have a thrust coefficient of $C_t = 0.12$ and provide a thrust of $T = 2.14$ N. The rotors are operated in stagnant air representing a hover scenario (thus the advance ratio is $J = 0$). Experiments are performed in an enclosure of $2 \times 3 \times 2$ m$^3$ at conditions of normalized tip-to-tip rotor spacing $S/R = [0.05, 1.0, 2.0]$ and normalized height $H/R = [1.0, 2.0, 3.0, 4.0]$. Experimental conditions are summarized in Table 1.

### B. Measurement Apparatus and Procedure

Volumetric velocity measurements cover the flow domain illustrated in Fig. 2. HFSBs generated under controlled conditions [26] are employed that scatter sufficient light in conditions of volume illumination and imaging. The suitability of this seeding technique for rotorcraft aerodynamics has been recently demonstrated in the study by Wolf et al. [27]. Two HFSB generators are used, producing

**Table 1 Two-rotor operating conditions**

| Rotor parameters and operation | |
|---|---|
| Rotation speed, $\Omega$ [Hz] | 167 |
| Number of blades, $B$ | 2 |
| Radius, $R$ [mm] | 76.2 |
| Chord Reynolds, $Re_c$ | 42,000 |
| Tip Mach, $M_{\text{tip}}$ | 0.22 |
| Lateral separation, $S/R$ (tip-to-tip) | 0.05–2 |
| Rotor-to-ground standoff distance, $H/R$ | 1–4 |
| Thrust, $T$ [N] | 2.14 |
| $C_t$ | 0.12 |

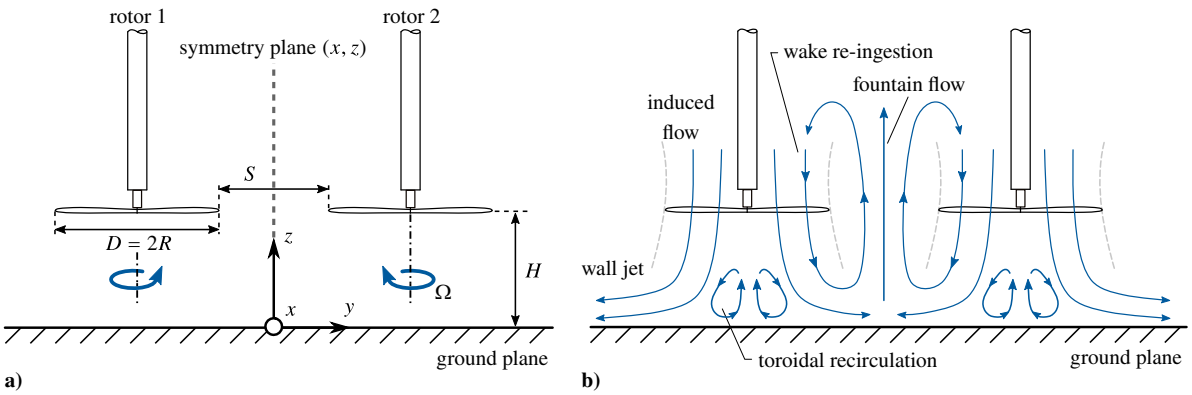


**Fig. 1 a) Schematic representation of the side-by-side rotor system in ground effect with relevant parameters and system of coordinates. b) Conceptual flow topology.**

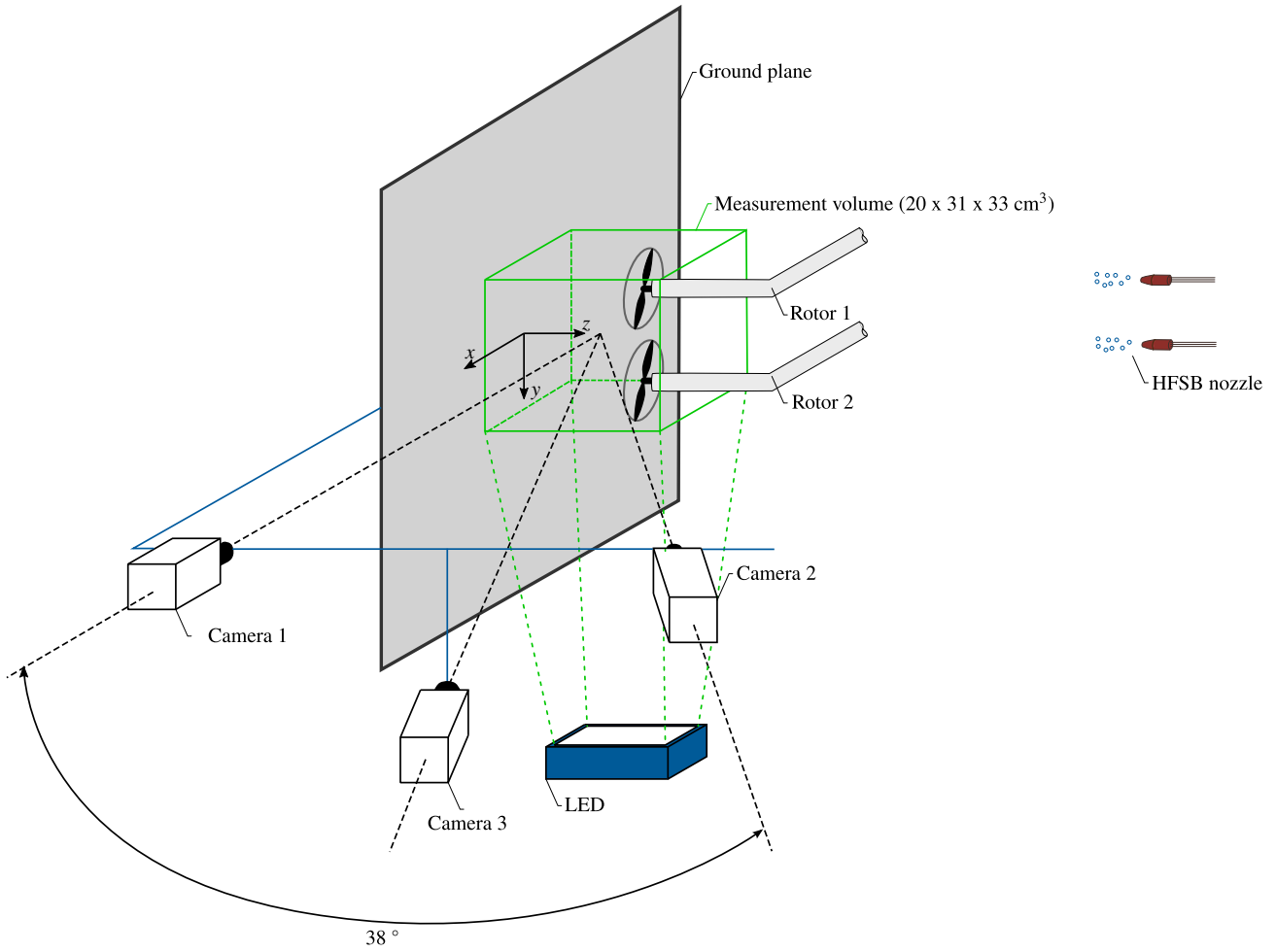


**Fig. 2 Three-dimensional schematic of the experimental apparatus, coordinate system, and measurement volume. The origin of the coordinate system is at the center location between the two rotors at the ground plane.**

each approximately 30,000 bubbles per second, with a mean diameter of 0.4 mm and nearly neutrally buoyant. The enclosure is seeded for 2 minutes before performing the measurement. The achieved seeding density is approximately 0.01 particles per pixel (ppp) corresponding to a spatial concentration of 0.5 particles/cm$^3$. The measurement volume is illuminated by a LaVision LED-Flashlight 300 device at a distance of 0.7 m below the measurement volume. Illumination is performed at a rate of 2.0 kHz, and the duration of illumination for each pulse (pulse width) is $\delta t = 50$ $\mu$s. A tomographic imaging setup is composed of three high-speed Complementary Metal–Oxide–Semiconductor (CMOS) cameras (Photron Fastcam SA1.1) placed outside the enclosure at a distance of 1 m from the measurement region. The cameras subtend a total angle of 38° (see Fig. 2) and are equipped with lenses of focal lengths $f =$ 60 mm (camera 2) and $f = 50$ mm (cameras 1 and 3), set at numerical aperture $f_\# = 16$. The resulting measurement volume spans $20 \times 31 \times 33$ cm$^3$ ($4.3R \times 4.0R \times 2.6R$). System synchronization is obtained with a LaVision Programmable Timing Unit (PTU 8), and each measurement comprises of 2000 recordings for a duration of 1 s. The object-to-image mapping parameters are obtained with a calibration procedure based on a target recorded at three positions separated by 10 cm each. The residual calibration disparity is reduced to less than 0.1 pixels using the volume self-calibration method [28]. An overview of the measurement parameters is presented in Table 2.

The raw footage from the cameras is first preprocessed using a high-pass frequency filter [29] that eliminates any stationary reflection from the ground plane and support struts of the rotors. As a second preprocessing step, the particle peak intensity is normalized and a Gaussian smoothing is applied. A comparison between a typical raw image and preprocessed one is presented in Fig. 3.

**Table 2 Illumination and imaging conditions**

| Measurement parameters | |
|---|---|
| $f$ [mm] | $1 \times 60$, $2 \times 50$ |
| $f_\#$ | 16 |
| Acquisition frequency [Hz] | 2000 |
| Sample time [s] | 1 |
| Pulse width [$\mu$s] | 50 |
| Particles per pixel | 0.01 |
| Field of view ($\Delta x$, $\Delta y$, $\Delta z$) | $20 \times 31 \times 33$ cm$^3$ |

### C. Lagrangian Particle Tracking

The 3D particle motion analysis is performed with the Shake-The-Box method [25]. The measurement delivers approximately 8000 particle tracks with a sampling frequency of 2.0 kHz. The maximum particle displacement within a particle track is approximately 20 pixels corresponding to a physical displacement of 6.4 mm. This particle displacement is comparable to other studies using the Shake-The-Box method and was shown to be adequate to capture the effect of individual blade passages by the rotors.

Data reduction to a Cartesian grid is performed following two different methods for the time-averaged and for the instantaneous velocity fields. Time-averaged information is gathered in cubic bins of 20 mm size with a 75% overlap factor, yielding a spacing of the velocity vectors of 5 mm. Every bin comprises approximately 10,000 samples. However, the concentration varies across the measurement domain. Nevertheless, a minimum number of 100 samples are set as a criterion for a valid measurement.

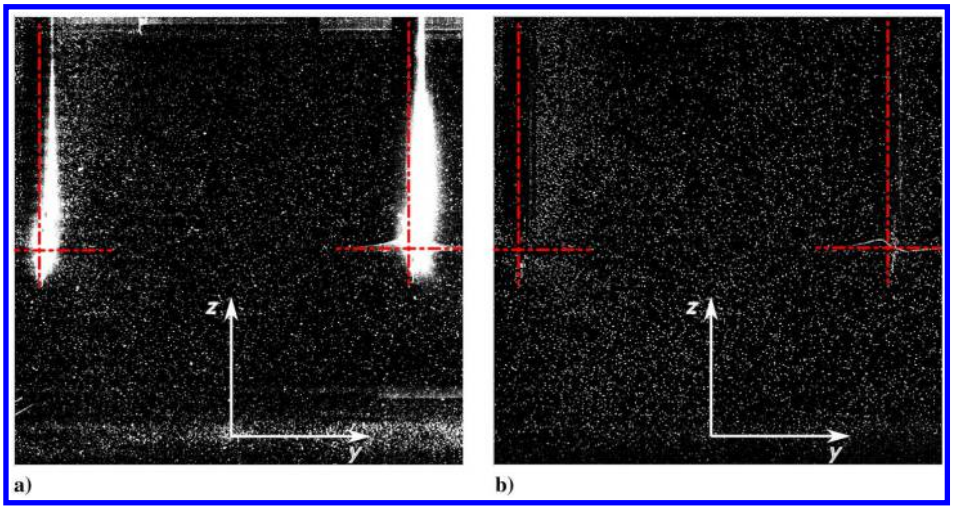


**Fig. 3 a) Extracted raw footage (1024 × 1024 pixels) of camera 1 in which LED light reflections of the rotor's support structure and ground plane are visible. b) Similar to (a) but after preprocessing the recording. Positions of the rotor axes and disks are given by the red dotted line.**



The instantaneous velocity fields are reconstructed using the vortex-in-cell technique (VIC+) as described by Schneiders and Scarano [30] for 3D scattered particle data; calculations are done in DaVis, with a modified algorithm (VIC # [31]). The instantaneous velocity field is reconstructed on a grid with $h = 7.5$ mm spacing between neighboring vectors.

The measurement dynamic spatial range (DSR), defined as the ratio between the largest and the smallest resolvable spatial wavelength, is estimated as the ratio between the domain larger size $L$ and the bin size. Values of DSR $= 66$ and DSR $= 44$ are obtained for the time-averaged and instantaneous velocity field, respectively. The dynamic velocity range (DVR) is estimated as the ratio between the maximum and minimum measured tracer velocity and is approximately equal to 360.

The measurement uncertainty $\epsilon_u$ for the time-averaged flowfield is statistically determined by the ratio between the relevant velocity fluctuations (axial velocity standard deviation) and the square root of the amount of samples per bin. The measurement uncertainty $\epsilon_u$ was below 0.5% of the rotor induced velocity in the majority of the domain, except for the shear layers along the boundary of the domain and close to the rotor blades, where it reaches up to $\epsilon_u = 1.5\%$.

## III. Time-Averaged Flowfields

When the rotor is operated in close proximity to the ground the wake expands radially. Figure 4 illustrates the difference in the velocity field, by the normalized axial velocity contours $w/W_{\text{ind}}$ and two-dimensional (2D) velocity vectors scaled by the velocity magnitude, for a single rotor with and without a ground plane. The former is considered at a distance of $2R$ above the ground (left plot of Fig. 4). The axial velocities are normalized by the induced velocity of an isolated rotor in hover ($W_{\text{ind}} = 14.25$ m/s), which is a constant and used for all results displaying velocity.

The rotor induces a downward velocity. The nonuniform velocity profile is due to hub wake leading to lower induced velocities along the rotor axis. For the isolated rotor, the slipstream contracts due to the increase in velocity. The maximum axial velocity is found at approximately 2 rotor radii below the rotor disk. Contradictory to this, the wake of a rotor in ground effect expands radially due to the pressure gradient caused by flow stagnation at the ground. Therefore, the axial velocity in the wake of the rotor in ground effect can be significantly lower compared to that of the unbounded rotor. At a certain height this is also noticed at the blade level, which results in an increased local blade angle and an increase in thrust for constant pitch. Also, characteristic for a single rotor in ground effect is the formation of a toroidal flow separation region, or so-called dead air region [14], below the rotor hub near the ground. This is caused by flow stagnation due to the lower velocities in the center of the slipstream and the adverse pressure gradient near the wall.

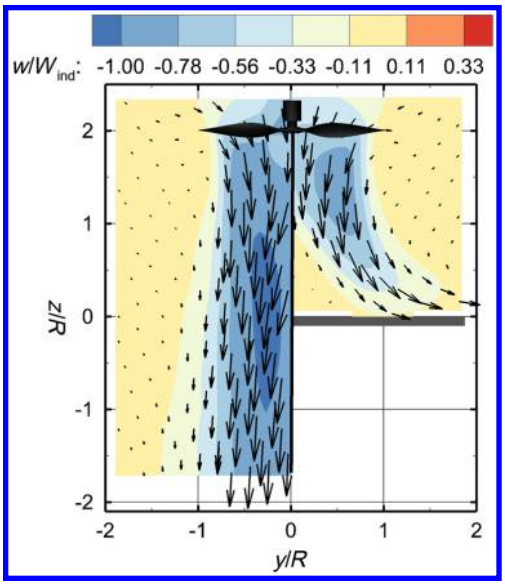


**Fig. 4 Comparison between the normalized time-averaged axial velocity contours and 2D velocity vectors of a single isolated rotor ($y/R < 0$) and a single rotor in ground effect ($y/R > 2$). For the latter, the ground plane is located at $z/R = 0$.**

When a second rotor is introduced, separated, for instance, by one rotor diameter, a fountain flow emerges. This is illustrated in Fig. 5a, by the axial velocity contours and velocity vectors in the plane through the rotor axes, for $H/R = 2$ and $S/R = 2$. The rotors produce two radial wall jets opposing each other with subsequent stagnation and separation from the wall near the symmetry plane, i.e., $y/R = 0$, where they redirect upward, ultimately generating the fountain pattern. The fountain flow rises above the disk plane in Fig. 5a, also sustained by the favorable pressure gradient determined by the rotor's suction. The wake appears to be mostly re-ingested by rotor 1, and a non-axial inflow condition for rotor 1 is observed. These inflow conditions cause more momentum to be transferred to the center of the slipstream and reduce the entity of the toroidal separation at the wall from rotor 1. The results in Fig. 5a illustrate that wake interactions in ground proximity occur at larger rotor separations compared to the interactions that take place during hover [8].

## IV. Rotor Spacing and Ground Proximity

The primary flow features of the side-by-side rotors are altered by the relative rotor spacing and distance to the ground. The effect of

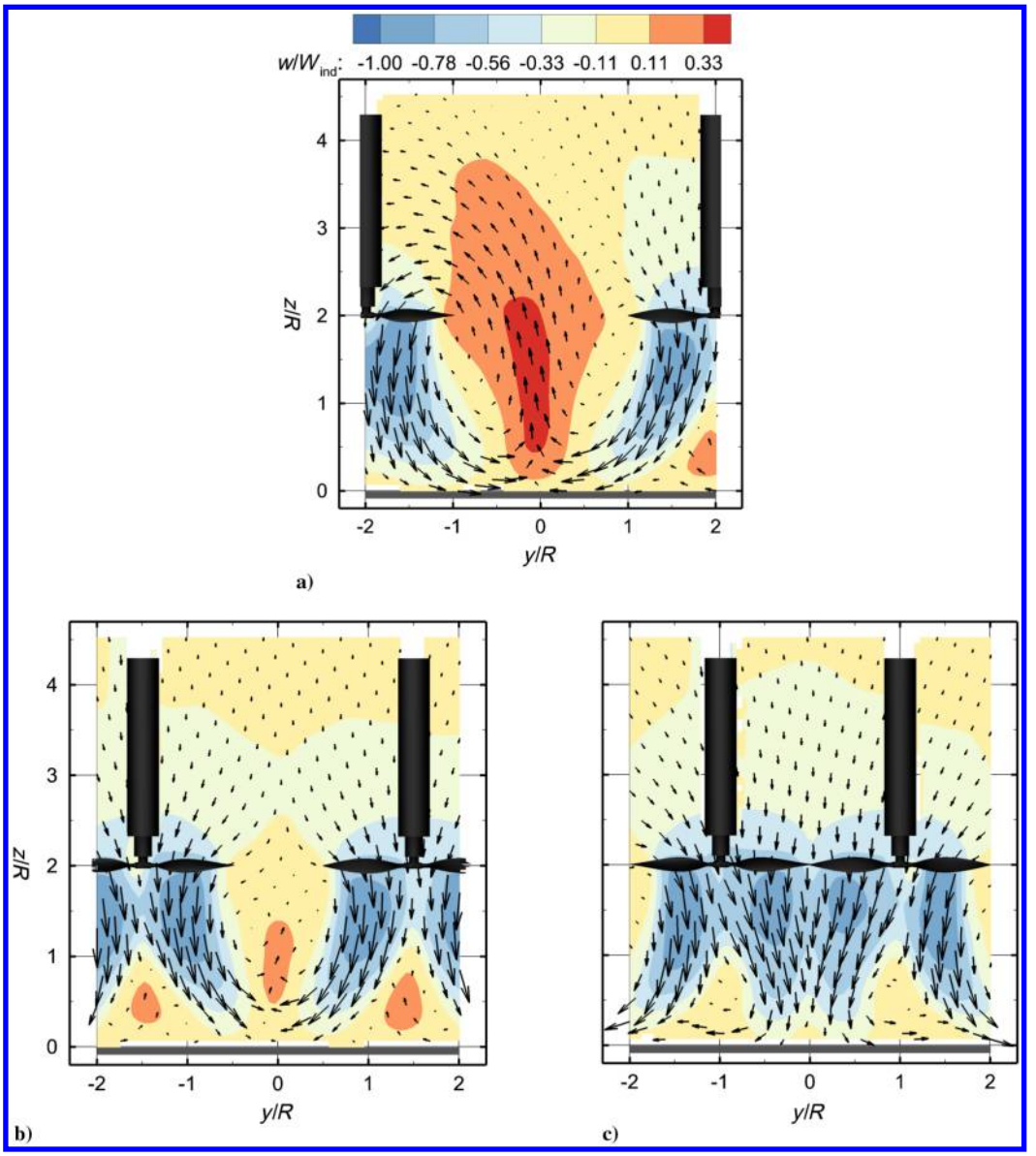


**Fig. 5 Normalized time-averaged axial velocity and 2D velocity vectors in the plane through the rotor axes ($x = 0$) at a rotor height of $H/R = 2$ for $S/R = 2$ (a), $S/R = 1$ (b), and $S/R = 0.05$ (c).**

these parameters on the fountain flow, the induced velocity, and the turbulent kinetic energy are examined hereafter.

### A. Rotor Spacing

By decreasing the lateral distance between the rotors, a stronger interaction between adjacent rotors is expected. However, a reduction of lateral spacing between the rotors is also associated with a decrease in the size of the fountain region for the various test conditions. This is illustrated in Fig. 5 by the axial velocity for $S/R = 1$ (b) and $S/R = 0.05$ (c), for a constant height of $H/R = 2$. This can therefore be compared to the case of $S/R = 2$, as presented in Fig. 5a.

Placing the rotors closer together, i.e., $S/R = 1$, means that the radial wall jets collide before they move parallel to the ground plane and more momentum is transferred out-of-plane rather than being redirected upward. This condition decreases the extent of the fountain flow that is visible for the plot of $S/R = 1$ (see Fig. 5b). The fountain flow, in this case, remains confined between the ground and the height of the rotor disks. Due to flow stagnation of the fountain flow, two recirculation regions are formed between each rotor wake and the tip of the fountain flow. No re-ingestion takes place, and a symmetric flowfield is produced in which each of the two wakes represents the wake of a single rotor in ground effect. This means that the toroidal separation regions near the ground are also present.

A different mechanism takes place when the rotor spacing is further reduced to $S/R = 0.05$. At this rotor separation distance, there is mutual induction of the individual rotor wakes, caused by the Coandă effect [7]. This happens before the wake interacts with the ground plane and therefore no fountain is created. A flowfield with lower induced velocities between the rotor axis is present due to the increased limitations of radial wake expansion in this region. Around the center of the domain close to the ground, i.e., ($y/R = 0$, $z/R = 0$), the wake moves laterally outward. A greater effect is observed on the separation regions below the rotor hub, which have now become separated from the ground. The shape of the separation region has been changed and only a single node is observed here. Similar to the case of $S/R = 1$, no wake re-ingestion occurs and a symmetrical mean velocity field is found.

To show the 3D evolution of the streamwise velocity component in the wake, the axial velocity contours $w/W_{\text{ind}}$ and 2D velocity vectors are extracted in the ($x$, $y$) plane at varying heights of $z/R =$ [0.3, 1.0, 1.7] and are presented in Fig. 6. At few positions the data are missing, due to optical blocking from the rotor's support. Also low particle intensity in the preprocessed images near the ground plane, i.e., $z/R = 0.3$, causes some local data dropout.

From the axial velocity extracted at the $z/R = 1.7$ plane, the top row of Fig. 6, it is possible to identify the effect on induced velocity

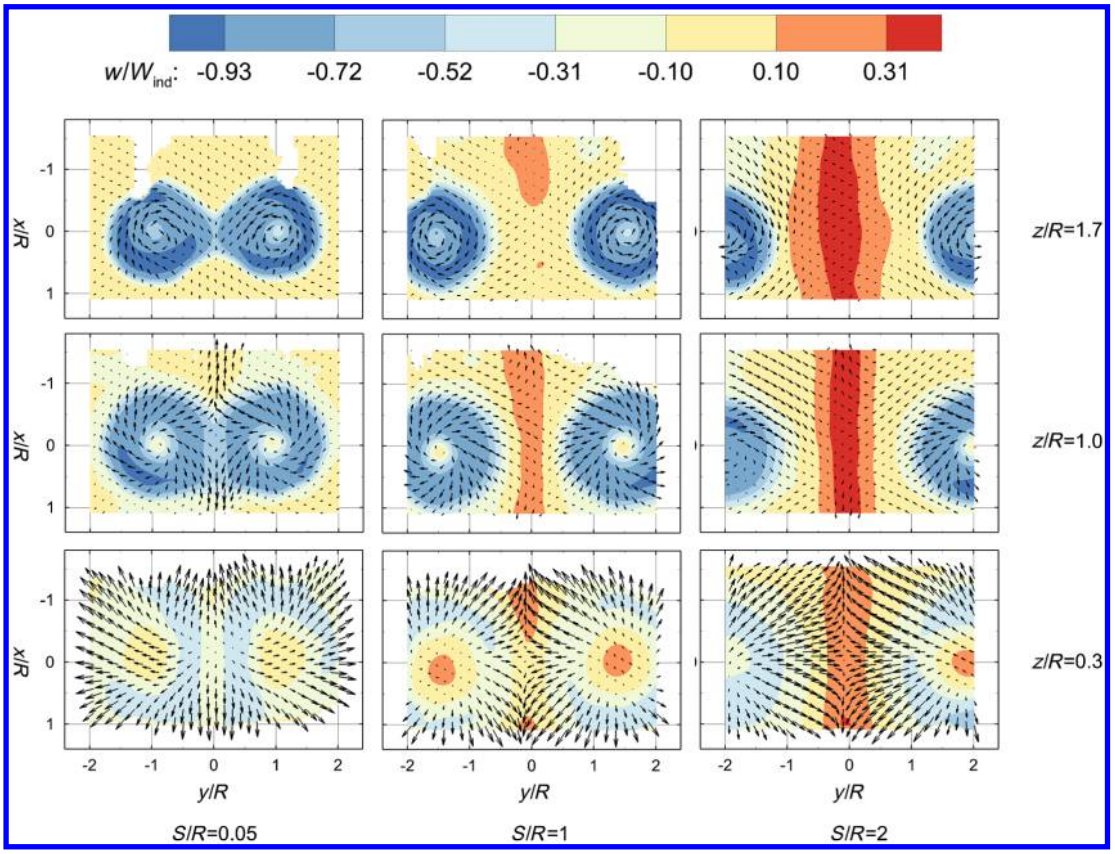


**Fig. 6 Normalized time-averaged axial velocity and 2D velocity vectors extracted at $z/R = 0.3$, $z/R = 1.0$, and $z/R = 1.7$ for the different values of the rotor spacing and $H/R = 2$.**

near the rotor blades that will have a direct influence on the rotors' performance. For the closest rotor spacing considered, i.e., $S/R = 0.05$, a non-axisymmetric wake profile for each of the two rotors is apparent; in the region between the rotor axes, there is a clear reduction in the axial velocity. Increasing the rotor spacing to $S/R = 1$ prevents any interaction between the two rotor wakes, and an axisymmetric induced velocity profile is restored. The fountain flow is also apparent between the two wakes but not affecting the rotor wake itself. When considering the larger rotor separation distance of $S/R = 2$, the top-right image of Fig. 6, the similarity of the two individual wakes is removed. Here, in the wake of rotor 1 for $S/R = 2$, rather than the typical swirl around the axis of rotation, the velocity vectors are directed toward the center of the wake. Moreover, in the flowfield surrounding the wake of the rotors, a stronger lateral component of the velocity is visible for $S/R = 2$, indicated by the larger velocity vectors, when compared to the other rotor separation distances. The velocity vectors are in the direction of a region between the rotors and the fountain flow and are ascribed to a low-pressure region.

Following the wake in streamwise direction to a height of $z/R = 1.0$, as presented in the middle row of Fig. 6, the radial expansion of the slipstream becomes apparent. This results in stronger mutual induction of the wakes for $S/R = 0.05$. Moreover, because one rotor wake obstructs the wake expansion of the other rotor, there is a strong velocity component in $x$ direction along $y/R = 0$, indicated by the large vectors. For $S/R = 1$, at this height in the wake, the fountain flow becomes apparent between the rotor wakes (see the middle plot of Fig. 6). However, there is little effect on the wake profile. For $S/R = 2$, the wake of rotor 1 has very weak radial velocities ascribed to the re-ingestion of the fountain. For this largest rotor spacing, the fountain is also considerably narrower compared to close to the blades, as it was in the plot of $z/R = 1.0$ (see top right of Fig. 6).

Close to the ground plane at $z/R = 0.3$, the bottom row of Fig. 6, the wake from the rotor has much lower axial velocity caused by the increase in static pressure. The axial velocity is transferred to velocities along the radial component, indicated by the larger vectors, which form the radial wall jets. In the case of $S/R = 0.05$, a single wall jet is directed outward along the center of the combined wake. For the $S/R = 1$ and $S/R = 2$, two radial wall jets are formed. The stagnation line is clearly visible by the positive axial velocity and the collision of the two rotor wall jets. However, for $S/R = 1$, there are higher axial velocities and lower radial velocities as the wall jet approaches the stagnation line. One should note that the stagnation line between the propellers has a slight offset toward the negative $y/R$-bound, which can be the cause of a minor misalignment of the setup or small geometric differences between the rotor blades.

Apart from the apparent differences in the mean velocity field, the velocity fluctuations are also influenced by the lateral spacing of the rotors. The unsteady flow behavior is statistically described by the normalized turbulent kinetic energy, $\mathrm{TKE} = 0.5(\overline{u'^2} + \overline{v'^2} + \overline{w'^2})/U_{\mathrm{tip}}^2$. Its spatial distribution is illustrated in Fig. 7. Fluctuations are concentrated along the tip vortex path and hub region, at $z/R = 1.7$. Regarding $S/R = 0.05$, there is a clear mutual induction of the tip vortex path creating a horseshoe-like TKE distribution in this plane. This loss of the structure of the tip vortices between the wakes complies with both experimental [7] and numerical studies [9] on side-by-side rotors out of ground effect. For the case of $S/R = 1$, the TKE values along the tip vortex path are similar compared to $S/R = 0.05$, but there are also relatively large values of TKE between the rotors in the fountain flow region. At the largest rotor separation distance of $S/R = 2$, the effect of flow re-ingestion on the velocity fluctuations becomes notable. Higher TKE levels are found in the wake of rotor 1, which is more severely subject to flow re-ingestion. This is visible along the tip vortex path and in the inner part of the slipstream. Regions of high TKE near the blades can indicate regions of unsteady loading, more pronounced force fluctuations, and broadband noise emissions [32].

The magnitude of the TKE decreases gradually for all rotor spacings due to viscous dissipation, which is visible in the $z/R = 1.0$ plane. Aside from the higher magnitude, overall TKE distribution

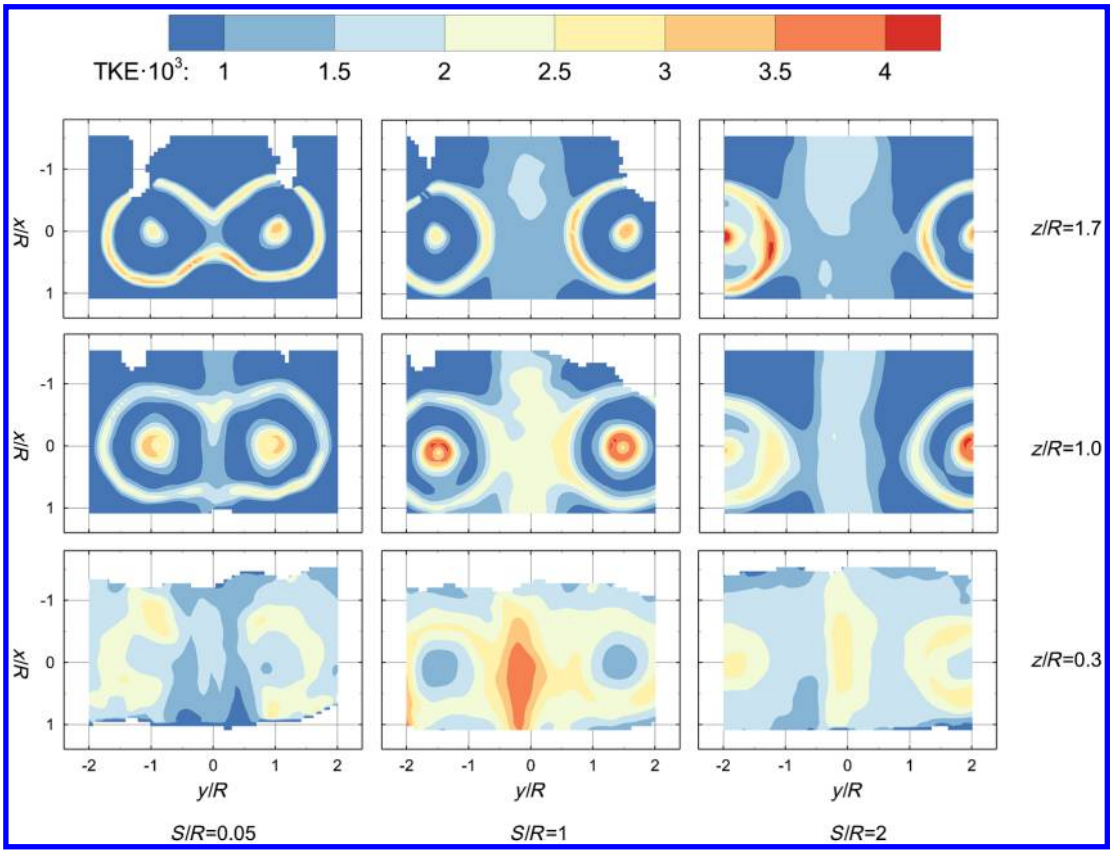


**Fig. 7 Three-dimensional distribution of normalized turbulent kinetic energy extracted at $z/R = 0.3$, $z/R = 1.0$, and $z/R = 1.7$ for the different values of the rotors spacing and $H/R = 2$.**

looks similar to what is observed near the blade. However, the TKE has increased in the fountain flow as well as below the rotor hub due to flow stagnation. Regarding $z/R = 0$, the overall levels of the TKE have increased but are distributed more uniformly in this plane. TKE between the rotors for $S/R = 0.05$ are low, whereas for rotor spacings of $S/R = 1$ and $S/R = 2$ there are typically higher values of TKE along the stagnation line. This is especially visible for $S/R = 1$, where higher TKE values are found near the stagnation line region compared to $S/R = 2$.

### B. Ground Proximity

Proximity to the ground induces an earlier deflection of the slipstream toward the wall jet. A more powerful interaction is therefore expected to occur in the region in between the rotors and with possibly more prominent effects of the fountain flow. Figure 8 illustrates such effects when $H/R$ is varied from 1 to 3 maintaining a constant rotor spacing $S/R$ of 2. Hence, the effect of the rotor height can therefore be analyzed by comparing this to Fig. 5a. At the lowest rotor height $H/R = 1$, there is a clear reduction of the induced velocity compared to the same system at $H/R = 2$ (see Fig. 5). Varying the rotor height does not alter the absolute height of the fountain flow. The re-ingestion of the ejected wall jet appears to be biased toward rotor 1, although the flow induced by both rotors appears to be similar. This can be explained by the fact that the process of wake re-ingestion happens further away from the rotors due to the constant size of the fountain flow. Consequently, the inflow conditions to rotor 1 are undisturbed and axial, creating slipstream characteristics that are similar for rotor 1 and rotor 2 and comparable to the single rotor case. Even though the velocities are lower below the rotor disk, the flow does not stagnate here but is rather in the direction toward the fountain. This in turn can be caused by the stronger wall jet at the inner region of the two wakes caused by the subatmospheric pressure of the fountain flow [33].

When larger ground standoff distances are considered, $H/R = 3$, the fountain flow decreases slightly in size but the process of flow re-ingestion happens closer to the rotor blades compared to what is observed in $H/R = 1$. This creates a more pronounced nonaxial direction of inflow to the rotors. Similar to the case of $H/R = 2$ (see Fig. 5a), an increase in induced velocity in the center of the wake is found. Flow re-ingestion is again biased toward rotor 1, which creates a flowfield that is highly asymmetric. Similar to the case of $H/R = 2$, the toroidal separation region at the ground is missing for rotor 1 and is visible for rotor 2. A recirculation zone is present between rotor 1 and the fountain at $(y/R, z/R) = (-0.75, -1.25)$.

### C. Summary of Identified Flow Regimes

The results of Secs. IV.A and IV.B can be combined to identify different flow regimes. These flow regimes can be placed on a map consisting of rotor spacing along the $x$ axis and rotor height along the $y$ axis, as presented in Fig. 9. From a high-level perspective, three different flow patterns have been identified within the parameter space that has been considered. One should note that the exact position of the boundaries between the different flow regimes is unknown and could change for different blade loading.

For close rotor spacing ($S/R = 0.05$), the wakes of the rotors move toward one another due to the Coandă effect. Hence, there is a flow attachment of the wakes before they interact with the ground. The combined wake then attaches to the ground and no fountain is generated. The induced velocity below the hub is still low, and therefore the flow stagnates here. However, only a single node is created that is separated from the ground. The high momentum at the inner part of the combined wake is also pushed out and flows below the separation regions toward the boundaries of the measurement domain. In this state the induced velocity between the rotor axes is lower compared to the outer part of the combined wake, which could result in a stronger influence of the thrust increase but can also offset unsteady loading on the blades. By increasing the rotor spacing, the Coandă effect is lost and the two separated rotor wakes interact with the ground plane. The wakes expand by the increase in pressure close to the ground and interact over a stagnation line. Over this stagnation

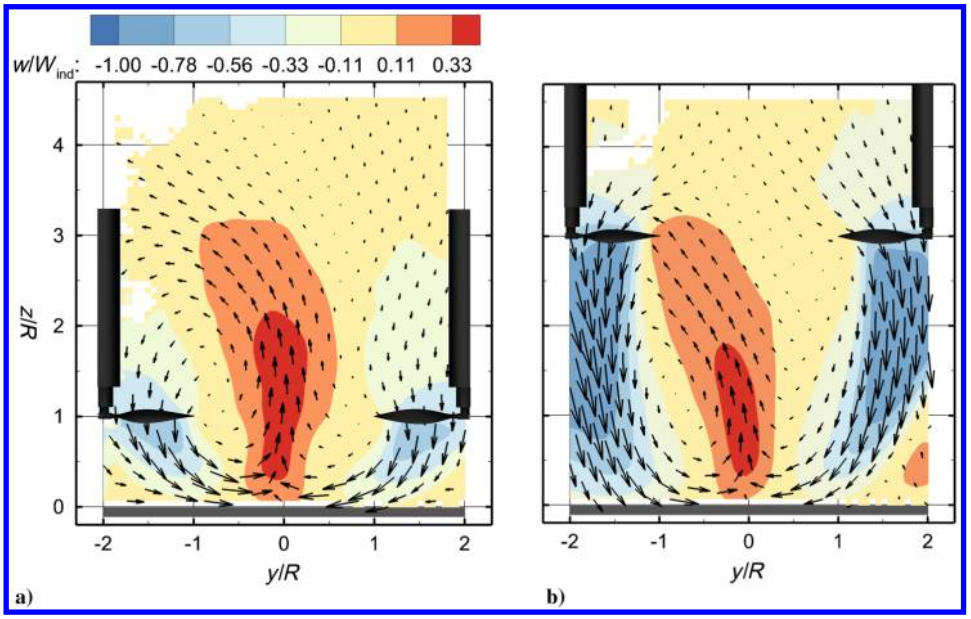


**Fig. 8 Normalized time-averaged axial velocity and 2D velocity vectors in the plane through the rotor axes ($x = 0$) for $H/R = 1$ (a) and $H/R = 3$ (b) for $S/R = 2$.**

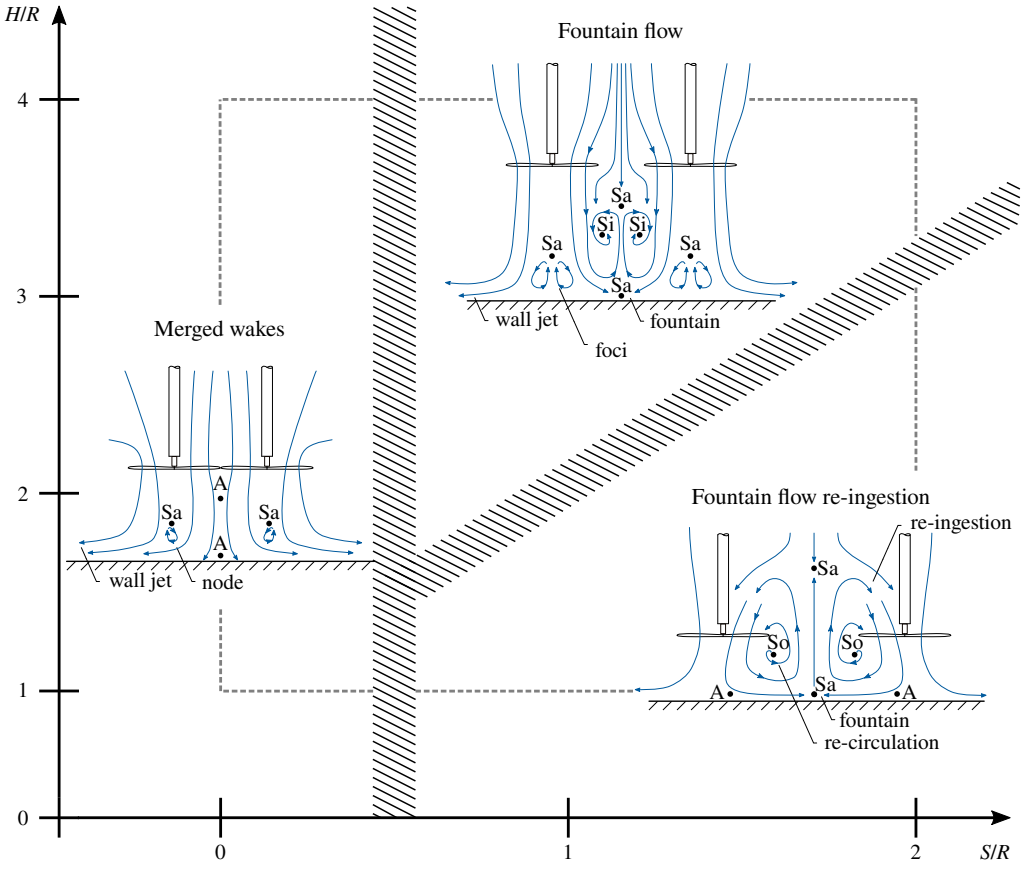


**Fig. 9 Observed flow regimes for a side-by-side in ground effect as a function of rotor height and rotor spacing with relevant flow features and critical points. Point A indicates a flow attachment point, So is a source, Si is a sink, and Sa is a saddle point. The gray dotted box represents the domain of the parameter space that was investigated.**

line the fountain flow is generated, the size of which is determined by the rotor spacing. If the wakes interact before the wall jet flows parallel to the ground plane, most of the momentum is pushed in- and out-of-plane. Consequently, for smaller rotor spacings and larger rotor heights, the fountain stays below the rotor disks. The individual wakes therefore strongly resemble the characteristics of a single rotor in ground effect.

At the largest rotor spacing investigated in the current study, the wall jet can develop over the ground plane. The wall jets interact head-on in the saddle point, which increases the size of the fountain. This increases the chance for the fountain to rise above the rotor disk, which has a dramatic effect on the slipstream characteristics. By re-ingestion the inflow becomes highly nonaxial, which could increase unsteady loading on the blades and reduce the efficiency. More

momentum is transferred to the center of the wake in the re-ingestion state. A consequence of the more uniform velocity distribution is the absence of a toroidal separation region above the ground. Furthermore, there is entrainment of air in the region between the rotors and the fountain, which causes recirculation.

## V. Temporal Dynamics of the Upward Fountain Flow Feature

As observed in the mean flow analysis, wake re-ingestion seems to be biased toward rotor 1, which violates the symmetry condition between the two rotors. Underlying in the mean velocity field are rich temporal phenomena, in particular for the fountain re-ingestion regime. The aim of this section is to highlight these temporal features by means of brief analysis. This is done by way of simple time series observations when considering the lateral (horizontal) velocity between the two rotors for the case of $H/R = 2$ and $S/R = 2$, as illustrated in Fig. 10.

For the duration of acquisition (1 s), the lateral velocity fluctuations $v'/W_{\text{ind}}$ between the rotors are primarily negative; this was earlier on observed in the asymmetric time-averaged flowfield yielding a negative $v/W_{\text{ind}}$ velocity at $(y/R, z/R) = (0, 2)$. When evaluating the time series, relatively large time-scale variations are evident and result in the lateral velocity being positive and negative at times. This suggests that the wake re-ingestion changes direction a number of times during the acquisition period that covered 333 blade passages in total. The switching in sign of the $v/W_{\text{ind}}$ velocity in between the rotors seems aperiodic, but the acquisition length of the current data set is too short for extracting conclusive statistics on this low-frequency temporal dynamics. Nevertheless, a few more observations can be made from the instantaneous spatial velocity fields.

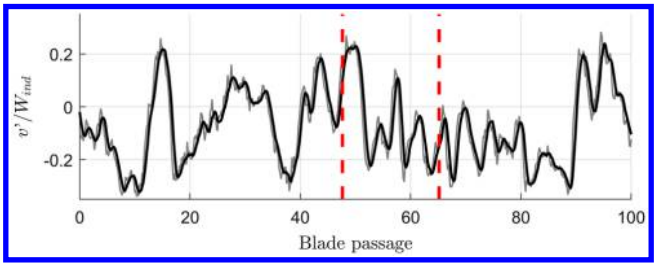


**Fig. 10 Segment of the time series of the normalized lateral velocity fluctuations $v/W_{\text{ind}}$ for $H/R = 2$ and $S/R = 2$ extracted between the rotors at $z/R = 2$. The raw time series is shown in grayscale, and a filtered version with a bandwidth moving filter of one blade passage is shown in black. The red dotted lines indicate the temporal instances for which the velocity fields are shown in Fig. 11.**

It is hypothesized that the wake re-ingestion changes direction over time, and this can be confirmed by extracting velocity fields at two different time instants. One time instant is associated with a positive lateral velocity, at blade passage 48, and the other time instant is associated with a negative lateral velocity between the rotors, at blade passage 65. The normalized axial velocity contours and 2D velocity vectors, scaled by the relative velocity magnitude, of these two time instants are presented in Fig. 11. A vector skip of four in both $y$ and $z$ directions is imposed for visibility reasons.

The instantaneous velocity fields of Fig. 11 confirm that the fountain flow wake re-ingestion has a coherent behavior and that the location and direction of the fountain plume move in time. At blade passage 48 (Fig. 11a), the fountain flow is oriented toward the rotor on the right, whereas at blade passage 65 (Fig. 11b), the opposite is observed. This switching is observed for a total of three times during the sample time of 1 s. Consequently, the timescale associated with this process is different compared to the blade passing frequency (BPF, $3.3 \cdot 10^{-3}$ s). Moreover, the switching does not seem to have a causal relation with the relative blade positioning, which takes place over a much longer periodic timescale of about 2 s. This therefore suggests that there are complicated flow interactions taking place, which causes this wake re-ingestion to drift in the lateral direction. These observations are in line with the aperiodic wake re-ingestion caused by wing–rotor interaction for a tilt-rotor configuration [34] and with a recent numerical investigation on a side-by-side rotor in ground effect [35]. However, an analysis of the dynamic behavior of the fountain flow was not within the scope of the current investigation. Consequently, the temporal dynamics of the wake interactions will be analyzed in a future study.

## VI. Conclusions

An experimental study with volumetric measurements obtained by Lagrangian particle tracking velocimetry using HFSBs has been carried out to investigate the rotor wake mean characteristics. This provided valuable insight in the 3D wake interactions of multirotors in ground effect.

Different flow regimes for a side-by-side rotor in ground effect have been identified. These flow regimes depend on a combination of rotor spacing and height over the ground plane. In closely spaced rotors, with a tip-to-tip spacing close to zero, the individual rotor

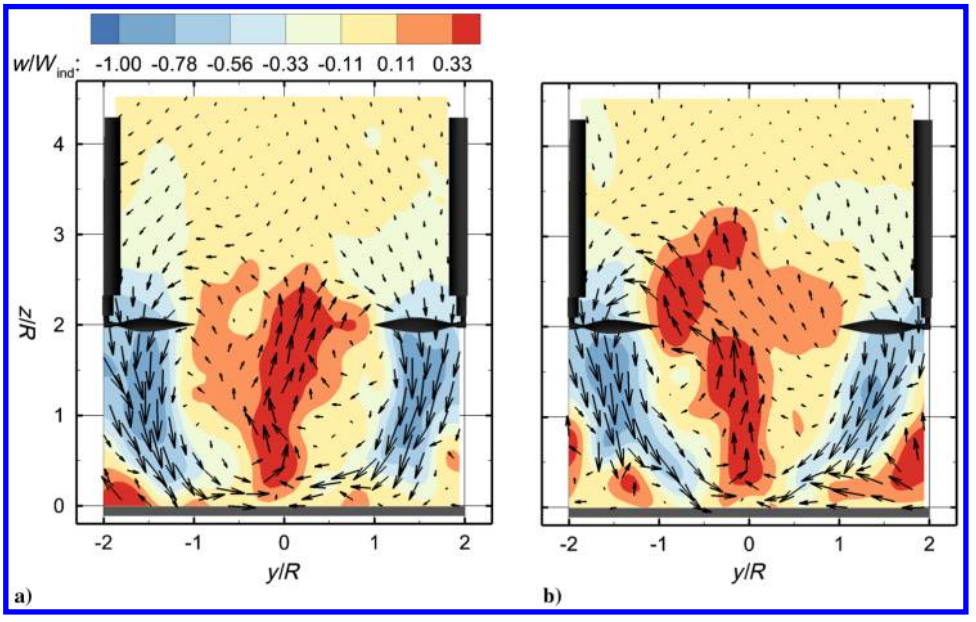


**Fig. 11 Normalized instantaneous axial velocity and 2D velocity vectors in the plane through the rotor axes ($x = 0$) extracted at blade passage 48 (a) and blade passage 65 (b) in the rotor plane for $H/R = 2$ and $S/R = 2$.**

wakes move laterally toward one another by the Coandă effect and form a combined wake before they interact with the ground plane. By increasing the rotor separation to tip-to-tip spacings of at least one rotor radius, an upward flow component known as the fountain flow is created over a line between the two rotors. The height of this fountain flow increases with increasing rotor separation. This can result in the fountain flow to rise above the rotor disk where it is re-ingested into the rotors. However, planar symmetry between the two rotors is lost because the wake re-ingestion is biased toward one of the rotors. In this wake re-ingestion state, the inflow conditions to the rotors are affected, which results in an increase in the amount of the unsteadiness near the rotor blades. This could introduce additional thrust fluctuations and broadband noise components. Moreover, wake re-ingestion increases the induced velocity of the rotor, which is especially noticeable in the center of the wake.

Decreasing the height decreases the induced velocity effectively for the multirotor system. However, the observed fountain flow is indifferent for the rotor heights observed in this study. At large rotor spacing and small rotor height, the fountain flow reaches a sufficient height over the rotor disk to be re-ingested relatively axially. The effects of the flow re-ingestion are most pronounced where the height of the fountain flow is comparable to the height of the rotors.

Even though the mean flow results show a velocity profile that is biased toward one of the two rotors, dynamic features are involved in the wake re-ingestion state that results in lateral shifting of the fountain flow. Moreover, the wake re-ingestion is shown to switch between the left and right rotors throughout acquisition.

The different flow regimes presented in this study are valuable to explain the observed differences in mean performance as seen in multirotor systems in ground effect. The identification of large-scale dynamic features caused by the wake interactions could be detrimental to the controllability of multirotor vehicles during takeoff and landing.

## Acknowledgments

This research is funded by the European Union's Horizon 2020 research and innovation program under grant agreement no. 860103, project Enabling Optimized Disruptive Airframe-Propulsion Integration Concepts (ENODISE).

## References

[1] Straubinger, A., Rothfeld, R., Shamiyeh, M., Büchter, K.-D., Kaiser, J., and Plötner, K. O., "An Overview of Current Research and Developments in Urban Air Mobility–Setting the Scene for UAM Introduction," *Journal of Air Transport Management*, Vol. 87, Aug. 2020, Paper 101852.
https://doi.org/10.1016/j.jairtraman.2020.101852

[2] Shukla, D., and Komerath, N., "Low Reynolds Number Multirotor Aerodynamic Wake Interactions," *Experiments in Fluids*, Vol. 60, No. 4, 2019, p. 77.
https://doi.org/10.1007/s00348-019-2724-3

[3] Shukla, D., and Komerath, N., "Multirotor Drone Aerodynamic Interaction Investigation," *Drones*, Vol. 2, No. 4, 2018, p. 43.
https://doi.org/10.3390/drones2040043

[4] Ramasamy, M., "Measurements Comparing Hover Performance of Single, Coaxial, Tandem, and Tilt-Rotor Configurations," *Proceedings of the AHS 69th Annual Forum*, Vol. 31, American Helicopter Soc., Alexandria, VA, 2013, p. 32.

[5] Ning, Z., "Experimental Investigations on the Aerodynamic and Aeroacoustic Characteristics of Small UAS Propellers," Ph.D. Thesis, Iowa State Univ., Ames, IA, 2018.

[6] Lee, H., and Lee, D. J., "Rotor Interactional Effects on Aerodynamic and Noise Characteristics of a Small Multirotor Unmanned Aerial Vehicle," *Physics of Fluids*, Vol. 32, No. 4, 2020, Paper 047107.
https://doi.org/10.1063/5.0003992

[7] Zhou, W., Ning, Z., Li, H., and Hu, H., "An Experimental Investigation on Rotor-to-Rotor Interactions of Small UAV Propellers," *35th AIAA Applied Aerodynamics Conference*, AIAA Paper 2017-3744, 2017.
https://doi.org/10.2514/6.2017-3744

[8] Yoon, S., Lee, H. C., and Pulliam, T. H., "Computational Analysis of Multi-Rotor Flows," *54th AIAA Aerospace Sciences Meeting*, AIAA Paper 2016-0812, 2016.
https://doi.org/10.2514/6.2016-0812

[9] Alvarez, E. J., and Ning, A., "High-Fidelity Modeling of Multirotor Aerodynamic Interactions for Aircraft Design," *AIAA Journal*, Vol. 58, No. 10, 2020, pp. 4385–4400.
https://doi.org/10.2514/1.J059178

[10] Landgrebe, A. J., "The Wake Geometry of a Hovering Helicopter Rotor and Its Influence on Rotor Performance," *Journal of the American Helicopter Society*, Vol. 17, No. 4, 1972, pp. 3–15.
https://doi.org/10.4050/JAHS.17.3

[11] Lee, T. E., Leishman, J. G., and Ramasamy, M., "Fluid Dynamics of Interacting Blade Tip Vortices with a Ground Plane," *Journal of the American Helicopter Society*, Vol. 55, No. 2, 2010, Paper 022005.
https://doi.org/10.4050/JAHS.55.022005

[12] Milluzzo, J. I., III, and Leishman, J. G., "Vortical Sheet Behavior in the Wake of a Rotor in Ground Effect," *AIAA Journal*, Vol. 55, No. 1, 2017, p. 24.
https://doi.org/10.2514/1.J054498

[13] Nathan, N., and Green, R., "The Flow Around a Model Helicopter Main Rotor in Ground Effect," *Experiments in Fluids*, Vol. 52, No. 1, 2012, pp. 151–166.
https://doi.org/10.1007/s00348-011-1212-1

[14] Fradenburgh, E. A., "The Helicopter and the Ground Effect Machine," *Journal of the American Helicopter Society*, Vol. 5, No. 4, 1960, pp. 24–33.
https://doi.org/10.4050/JAHS.5.4.24

[15] Sanchez-Cuevas, P., Heredia, G., and Ollero, A., "Characterization of the Aerodynamic Ground Effect and its Influence in Multirotor Control," *International Journal of Aerospace Engineering*, Vol. 2017, Aug. 2017, pp. 1–17.
https://doi.org/10.1155/2017/1823056

[16] He, X., and Leang, K. K., "Quasi-Steady In-Ground-Effect Model for Single and Multirotor Aerial Vehicles," *AIAA Journal*, Vol. 58, No. 12, 2020, pp. 5318–5331.
https://doi.org/10.2514/1.J059223.

[17] Conyers, S. A., Rutherford, M. J., and Valavanis, K. P., "An Empirical Evaluation of Ground Effect for Small-Scale Rotorcraft," *2018 IEEE International Conference on Robotics and Automation (ICRA)*, Inst. of Electrical and Electronics Engineers, New York, 2018, pp. 1244–1250.
https://doi.org/10.1109/ICRA.2018.8461035

[18] Cheeseman, I., and Bennett, W., "The Effect of the Ground on a Helicopter Rotor in Forward Flight," Aeronautical Research Council TR 3021, 1957.

[19] Sharf, I., Nahon, M., Harmat, A., Khan, W., Michini, M., Speal, N., Trentini, M., Tsadok, T., and Wang, T., "Ground Effect Experiments and Model Validation with Draganflyer X8 Rotorcraft," *2014 International Conference on Unmanned Aircraft Systems (ICUAS)*, Inst. of Electrical and Electronics Engineers, New York, 2014, pp. 1158–1166.
https://doi.org/10.1109/ICUAS.2014.6842370.

[20] Wojno, J. P., Mueller, T. J., and Blake, W. K., "Turbulence Ingestion Noise, Part 1: Experimental Characterization of Grid-Generated Turbulence," *AIAA Journal*, Vol. 40, No. 1, 2002, pp. 16–25.
https://doi.org/10.2514/2.1636

[21] Zagaglia, D., Giuni, M., and Green, R. B., "Rotor-Obstacle Aerodynamic Interaction in Hovering Flight: An Experimental Survey," *Proceedings of the AHS International 72nd Annual Forum*, American Helicopter Soc., Fairfax, VA, 2016, pp. 1–9.

[22] Radhakrishnan, A., "An Experimental Investigation of Ground Effect on a Quad Tilt Rotor in Hover and Low Speed Forward Flight," Ph.D. Thesis, Univ. of Maryland, College Park, MD, 2006.

[23] Chirico, G., Szubert, D., Vigevano, L., and Barakos, G. N., "Numerical Modelling of the Aerodynamic Interference Between Helicopter and Ground Obstacles," *CEAS Aeronautical Journal*, Vol. 8, No. 4, 2017, pp. 589–611.
https://doi.org/10.1007/s13272-017-0259-y

[24] Scarano, F., Ghaemi, S., Caridi, G. C. A., Bosbach, J., Dierksheide, U., and Sciacchitano, A., "On the Use of Helium-Filled Soap Bubbles for Large-Scale Tomographic PIV in Wind Tunnel Experiments," *Experiments in Fluids*, Vol. 56, No. 2, 2015, pp. 1–12.
https://doi.org/10.1007/s00348-015-1909-7

[25] Schanz, D., Gesemann, S., and Schröder, A., "Shake-The-Box: Lagrangian Particle Tracking at High Particle Image Densities," *Experiments in Fluids*, Vol. 57, No. 5, 2016, pp. 1–27.
https://doi.org/10.1007/s00348-016-2157-1

[26] Faleiros, D. E., Tuinstra, M., Sciacchitano, A., and Scarano, F., "Generation and Control of Helium-Filled Soap Bubbles for PIV," *Experiments in Fluids*, Vol. 60, No. 3, 2019, pp. 1–17.
https://doi.org/10.1007/s00348-019-2687-4

[27] Wolf, C. C., Schwarz, C., Kaufmann, K., Gardner, A. D., Michaelis, D., Bosbach, J., Schanz, D., and Schröder, A., "Experimental Study of Secondary Vortex Structures in a Rotor Wake," *Experiments in Fluids*,

Vol. 60, No. 11, 2019, pp. 1–16.
https://doi.org/10.1007/s00348-019-2807-1

[28] Wieneke, B., "Volume Self-Calibration for 3D Particle Image Velocimetry," *Experiments in Fluids*, Vol. 45, No. 4, 2008, pp. 549–556.
https://doi.org/10.1007/s00348-008-0521-5

[29] Sciacchitano, A., and Scarano, F., "Elimination of PIV Light Reflections Via a Temporal High Pass Filter," *Measurement Science and Technology*, Vol. 25, No. 8, 2014, Paper 084009.
https://doi.org/10.1088/0957-0233/25/8/084009

[30] Schneiders, J. F., and Scarano, F., "Dense Velocity Reconstruction from Tomographic PTV with Material Derivatives," *Experiments in Fluids*, Vol. 57, No. 9, 2016, pp. 1–22.
https://doi.org/10.1007/s00348-016-2225-6

[31] Jeon, Y. J., Müller, M., Michaelis, D., and Wieneke, B., "Efficient Reconstruction of Flow Field with Pressure from Particle Tracks: VIC," *Bulletin of the American Physical Society*, Vol. 63, Nov. 2018.

[32] Carolus, T., Schneider, M., and Reese, H., "Axial Flow Fan Broad-Band Noise and Prediction," *Journal of Sound and Vibration*, Vol. 300, Nos. 1–2, 2007, pp. 50–70.
https://doi.org/10.1016/j.jsv.2006.07.025

[33] Abbott, W., and White, D., "The Effect of Nozzle Pressure Ratio on the Fountain Formed Between Two Impinging Jets," Royal Aircraft Establishment TR P1166, 1989.

[34] Polak, D. R., Rehm, W., and George, A. R., "Effects of an Image Plane on the Tiltrotor Fountain Flow," *Journal of the American Helicopter Society*, Vol. 45, No. 2, 2000, pp. 90–96.
https://doi.org/10.4050/JAHS.45.90

[35] Healy, R., McCauley, J., Gandhi, F., Sahni, O., and Mistry, M., "A Computational Investigation of Side-by-Side Rotors in Ground Effect," *Proceedings of the 77th VFS Annual Forum (Virtual)*, Vertical Flight Soc., 2021.

A. R. Jones
*Associate Editor*